

Compositional and phase dependence of elastic modulus of crystalline and amorphous $\text{Hf}_{1-x}\text{Zr}_x\text{O}_2$ thin films ^{EP}

Cite as: Appl. Phys. Lett. **118**, 102901 (2021); <https://doi.org/10.1063/5.0044702>

Submitted: 18 January 2021 . Accepted: 20 February 2021 . Published Online: 08 March 2021

 Shelby S. Fields,  David H. Olson,  Samantha T. Jaszewski,  Chris M. Fancher, Sean W. Smith,  Diane A. Dickie,  Giovanni Esteves, M. David Henry,  Paul S. Davids,  Patrick E. Hopkins, and  Jon F. Ihlefeld

COLLECTIONS

 This paper was selected as an Editor's Pick



View Online



Export Citation



CrossMark

ARTICLES YOU MAY BE INTERESTED IN

[Nonlinear domain wall velocity in ferroelectric Si-doped \$\text{HfO}_2\$ thin film capacitors](#)

Applied Physics Letters **118**, 102902 (2021); <https://doi.org/10.1063/5.0035753>

[Ferroelectric polarization retention with scaling of \$\text{Hf}_{0.5}\text{Zr}_{0.5}\text{O}_2\$ on silicon](#)

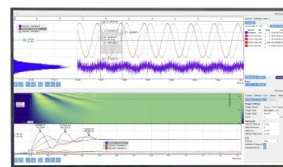
Applied Physics Letters **118**, 102903 (2021); <https://doi.org/10.1063/5.0035579>

[Next generation ferroelectric materials for semiconductor process integration and their applications](#)

Journal of Applied Physics **129**, 100901 (2021); <https://doi.org/10.1063/5.0037617>

Challenge us.

What are your needs for periodic signal detection?



Zurich Instruments

Compositional and phase dependence of elastic modulus of crystalline and amorphous $\text{Hf}_{1-x}\text{Zr}_x\text{O}_2$ thin films

Cite as: Appl. Phys. Lett. **118**, 102901 (2021); doi: [10.1063/5.0044702](https://doi.org/10.1063/5.0044702)

Submitted: 18 January 2021 · Accepted: 20 February 2021 ·

Published Online: 8 March 2021












View Online



Export Citation



CrossMark

Shelby S. Fields,¹  David H. Olson,²  Samantha T. Jaszewski,¹  Chris M. Fancher,³  Sean W. Smith,^{4,a)} Diane A. Dickie,^{1,5}  Giovanni Esteves,⁴  M. David Henry,⁴ Paul S. Davids,⁴  Patrick E. Hopkins,^{1,2,6}  and Jon F. Ihlefeld^{1,7,b)} 

AFFILIATIONS

¹Department of Materials Science and Engineering, University of Virginia, Charlottesville, Virginia 22904, USA

²Department of Mechanical and Aerospace Engineering, University of Virginia, Charlottesville, Virginia 22904, USA

³Materials Science and Technology Division, Oak Ridge National Laboratory, Oak Ridge, Tennessee 37831, USA

⁴Sandia National Laboratories, Albuquerque, New Mexico 87185, USA

⁵Department of Chemistry, University of Virginia, Charlottesville, Virginia 22904, USA

⁶Department of Physics, University of Virginia, Charlottesville, Virginia 22904, USA

⁷Charles L. Brown Department of Electrical and Computer Engineering, University of Virginia, Charlottesville, Virginia 22904, USA

^{a)}Present address: Radiant Technologies, Albuquerque, NM, USA.

^{b)}Author to whom correspondence should be addressed: jihlefeld@virginia.edu

ABSTRACT

The elastic moduli of amorphous and crystalline atomic layer-deposited $\text{Hf}_{1-x}\text{Zr}_x\text{O}_2$ (HZO, $x = 0, 0.31, 0.46, 0.79, 1$) films prepared with TaN electrodes on silicon substrates were investigated using picosecond acoustic measurements. The moduli of the amorphous films were observed to increase between 211 ± 6 GPa for pure HfO_2 and 302 ± 9 GPa for pure ZrO_2 . In the crystalline films, it was found that the moduli increased upon increasing the zirconium composition from 248 ± 6 GPa for monoclinic HfO_2 to 267 ± 9 GPa for tetragonal ZrO_2 . Positive deviations from this increase were observed for the $\text{Hf}_{0.69}\text{Zr}_{0.31}\text{O}_2$ and $\text{Hf}_{0.54}\text{Zr}_{0.46}\text{O}_2$ compositions, which were measured to have moduli of 264 ± 8 GPa and 274 ± 8 GPa, respectively. These two compositions contained the largest fractions of the ferroelectric orthorhombic phase, as assessed from polarization and diffraction data. The biaxial stress states of the crystalline films were characterized through $\sin^2(\psi)$ x-ray diffraction analysis. The in-plane stresses were all found to be tensile and observed to increase with the increasing zirconium composition, between 2.54 ± 0.6 GPa for pure HfO_2 and 5.22 ± 0.5 GPa for pure ZrO_2 . The stresses are consistent with large thermal expansion mismatches between the HZO films and silicon substrates. These results demonstrate a device-scale means to quantify biaxial stress for investigation on its effect on the ferroelectric properties of hafnia-based materials.

Published under license by AIP Publishing. <https://doi.org/10.1063/5.0044702>

Since the first report of ferroelectric responses nearly a decade ago,¹ HfO_2 -based thin films have witnessed research and development for applications including ferroelectric random access memory,^{2–5} energy harvesting,^{6,7} and negative differential capacitance field effect transistors.^{8,9} The ferroelectric response has been attributed to a non-centrosymmetric orthorhombic phase (space group $Pca2_1$), which is energetically metastable between the room-temperature, linear dielectric monoclinic ($P2_1/c$) and high-temperature field-induced ferroelectric tetragonal ($P42_1/mc$) phases.^{10,11} The stability of this

orthorhombic phase has been attributed to small crystallite sizes,¹² inclusion of specific dopants,^{13,14} and the presence of biaxial stress,^{15,16} among others. HfO_2 -based ferroelectrics are typically grown to thicknesses of 5–20 nm, which limits the grain size via thickness truncation, and doped to enhance orthorhombic phase stability. ZrO_2 alloying has been observed to stabilize the orthorhombic phase through a broad composition window ($x \approx 0.1–0.8$)^{17,18} and result in a reduced thermal budget compared to many other ferroelectric HfO_2 compositions.^{19,20} In spite of the many mechanisms to increase orthorhombic phase

stability, $\text{Hf}_{1-x}\text{Zr}_x\text{O}_2$ (HZO) thin films often exhibit mixtures of the orthorhombic, tetragonal, and monoclinic phases, with Hf-rich and Zr-rich compositions, resulting in monoclinic-rich and tetragonal-rich phase constitutions, respectively.^{17,18,21,22}

Biaxial stress impacts both the phase stability and the domain structure. Computational works have suggested that compressive biaxial stresses facilitate stabilization of the orthorhombic phase compared to the equilibrium monoclinic.¹¹ Experimental studies, alternatively, have observed enhanced polarization responses under conditions that yield biaxial tensile stress^{16,23} or favorable texture,²⁴ both of which alter the domain structure to maximize the degree to which the short polar axis is oriented normal to the film surface. Such experimental works examining stress effects in HfO_2 -based ferroelectrics rely on combinations of experimental and computationally predicted bulk elastic constants for the monoclinic, tetragonal, and orthorhombic phases for analysis. The measurement of these values in planar, mixed phase thin films is important because utilization of bulk, phase-pure elastic constants may discount effects of microstructural features such as the high density of grain boundaries and presence of interface segregated phases,^{18,25} both of which may affect the elastic properties. Thus, the direct measurement of elastic constants in relevant phases and phase mixtures present in HZO thin films provides necessary information for investigations of stress effects on phase stabilization, domain structure, and ferroelectric performance. Additionally, knowledge of the elastic behavior of these ferroelectric materials is critical for emergent piezoMEMS applications, such as resonator device structures.^{26,27}

In this study, the elastic moduli (E) of amorphous and crystalline 20 nm-thick $\text{Hf}_{1-x}\text{Zr}_x\text{O}_2$ ($0 \leq x \leq 1$) thin films prepared with TaN electrodes on silicon substrates are directly investigated using picosecond acoustic measurements. The crystallized films comprise pure monoclinic HfO_2 , pure tetragonal ZrO_2 , and phase mixtures in the alloy compositions, which include the ferroelectric orthorhombic phase. The experimental elastic moduli from these measurements are utilized to quantify the stress states of the crystalline 20 nm-thick HZO films through $\sin^2(\psi)$ x-ray diffraction analyses.

Metal-Insulator-Metal (MIM) devices comprising $\text{Hf}_{1-x}\text{Zr}_x\text{O}_2$, with $x = 0, 0.31, 0.46, 0.79$, and 1, between TaN top and bottom electrodes were prepared. 100 nm-thick TaN bottom electrodes were deposited via DC sputtering from a TaN target onto (001)-oriented silicon substrates under an argon background pressure of 5 mTorr at a power density of 3.3 W cm^{-2} with a 45° off-axis geometry. 20 nm-thick $\text{Hf}_{1-x}\text{Zr}_x\text{O}_2$ films were deposited via plasma-enhanced atomic layer deposition (PEALD) at a substrate temperature of 260°C using tetrakis(ethylmethylamido)hafnium (TEMA Hf) and tetrakis(ethylmethylamido)zirconium (TEMA Zr) as hafnium and zirconium precursors, respectively, and an oxygen plasma as the oxidant within an Oxford FlexAL II instrument, as detailed in the [supplementary material](#). The ratio of Hf:Zr cycles within each 10-cycle super cycle was altered to control the film composition. The growth rates were determined to be 1.05 \AA/cycle and 1.15 \AA/cycle for HfO_2 and ZrO_2 , respectively. Film compositions were determined via x-ray photoelectron spectroscopy measurements of fully processed devices, with details provided in the [supplementary material](#). Following HZO deposition, films meant for crystallization received planar, sputtered 20 nm-thick TaN top electrodes and the samples were annealed at 600°C for 30 s under N_2 at atmospheric pressure. Following annealing, samples on which electrical analyses were to be performed

received 50 nm-thick circular Pd contacts through a shadow mask with diameters spanning $100\text{--}500 \mu\text{m}$ via DC sputtering utilizing the same conditions as for the electrodes. Samples were subsequently exposed to an SC-1 etch solution (5:1:1 H_2O :30% H_2O_2 in H_2O :30% NH_4OH in H_2O) at 60°C for 25 min to remove the exposed TaN and define devices for electrical analyses using the Pd contacts as a hard mask. Polarization vs electric field hysteresis [$P(E)$, 10 ms test period], current-voltage, and positive up negative down (PUND, 1 ms pulse and 1000 ms delay) measurements were made between 1.0 and 2.5 MV cm^{-1} using a Radiant Technologies Precision LC II Tester. Capacitance-voltage (CV) measurements were performed using a Keysight E4980A LCR meter at 10 kHz with an oscillator amplitude of 50 mV. The phase constitution and thickness/density of each of the films were examined using grazing incidence x-ray diffraction (GIXRD) and x-ray reflectivity (XRR), respectively, on samples processed without Pd contacts using a Rigaku SmartLab diffractometer with Cu $K\alpha$ radiation in a parallel beam configuration. GIXRD was performed with the ω value fixed at 0.7° , and XRR patterns were fit using GSAS-II software.²⁸ 80 nm of aluminum was e-beam evaporated onto each film, which had been measured using GIXRD and XRR to serve as a transducer for picosecond acoustic measurements. The resulting acoustic signatures were fit using LIPRAS line-profile analysis software.²⁹ 2D diffraction patterns were collected on crystallized samples using a Bruker APEXII Duo diffractometer equipped with an Incoatec I μS Cu $K\alpha$ microfocus source and an APEXII CCD area detector with the ω value fixed at 18° . MgO powder was placed on film surfaces for use as a stress-free standard and for sample displacement alignment. Area detector patterns were unwarped using the pyFAI azimuthal integration package.³⁰ $\sin^2(\psi)$ analyses were carried out on the crystallized films using intensity profiles extracted at ψ angles between 0° and 45° relative to the film surface normal to calculate the stress state of each film using the elastic moduli determined from picosecond acoustic measurements.

Figure 1(a) shows the $P(E)$ response measured on each HZO film. Responses were observed to be linear for HfO_2 and ZrO_2 , hysteretic for $\text{Hf}_{0.69}\text{Zr}_{0.31}\text{O}_2$ and $\text{Hf}_{0.54}\text{Zr}_{0.46}\text{O}_2$, and pinched hysteretic for $\text{Hf}_{0.21}\text{Zr}_{0.79}\text{O}_2$. The largest polarization was observed for the $\text{Hf}_{0.54}\text{Zr}_{0.46}\text{O}_2$ film. The pure ZrO_2 film required electric fields in excess of 2.5 MV cm^{-1} to exhibit the typical field-induced ferroelectric response. Corresponding switching current measurements are available in the [supplementary material](#), Fig. S1. The remanent

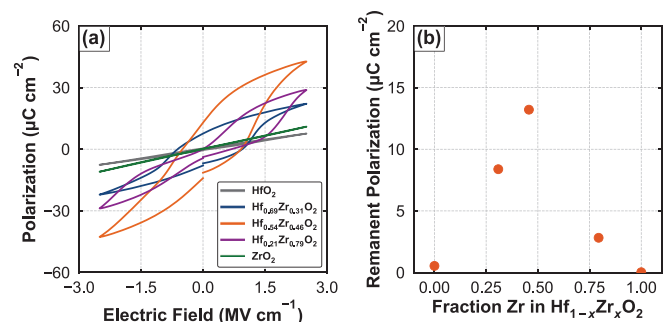


FIG. 1. (a) $P(E)$ measurements of HfO_2 (gray), $\text{Hf}_{0.69}\text{Zr}_{0.31}\text{O}_2$ (blue), $\text{Hf}_{0.54}\text{Zr}_{0.46}\text{O}_2$ (orange), $\text{Hf}_{0.21}\text{Zr}_{0.79}\text{O}_2$ (purple), and ZrO_2 (green) films. (b) P_r extracted from PUND measurements.

polarizations (P_r from PUND measurements at 2.5 MV cm^{-1}) for each composition within the series are shown in Fig. 1(b) and confirm the composition dependence of polarization observed in the $P(E)$ data. These responses are consistent with previous reports on the compositional dependence of the polarization response in HZO and suggest non-trivial orthorhombic phase fractions in the $\text{Hf}_{0.69}\text{Zr}_{0.31}\text{O}_2$ and $\text{Hf}_{0.54}\text{Zr}_{0.46}\text{O}_2$ films.^{17,18,21}

Figure 2 shows GIXRD patterns corresponding to each crystallized film, indicating the phases present at each composition. The diffraction pattern measured on the pure HfO_2 film contained two peaks at 28.6° and 31.9° in 2θ , which were indexed as the (111) and (111) monoclinic (m) reflections, respectively. Diffraction patterns measured on the $\text{Hf}_{0.69}\text{Zr}_{0.31}\text{O}_2$ and $\text{Hf}_{0.54}\text{Zr}_{0.46}\text{O}_2$ films contained an additional peak at 30.7° in 2θ , which was indexed as the superimposed (101) tetragonal/(111) orthorhombic (t/o) reflections and observed to increase in intensity with the increasing ZrO_2 concentration. The diffraction patterns measured on the $\text{Hf}_{0.21}\text{Zr}_{0.79}\text{O}_2$ and pure ZrO_2 films contained only t/o peaks. The t/o peak position increased in the diffraction angle in the ZrO_2 pattern, which is consistent with previous observations of the diffraction behavior in composition-varied HZO thin films and has been attributed to the tetragonal phase.¹⁹ GIXRD patterns for the un-annealed films lacked distinct Bragg reflections and are available in the supplementary material, Fig. S2. Together, the GIXRD patterns and electrical measurements suggest that the $\text{Hf}_{0.54}\text{Zr}_{0.46}\text{O}_2$ film contained the largest orthorhombic phase content: it exhibited the highest measured P_r and an intense, low angle t/o diffraction peak. The $\text{Hf}_{0.69}\text{Zr}_{0.31}\text{O}_2$ film, which had the second highest P_r and diffraction peaks corresponding to all three phases, likely had the second largest orthorhombic phase content. The $\text{Hf}_{0.21}\text{Zr}_{0.79}\text{O}_2$ film had a higher content of the tetragonal phase, as evidenced by the pinched hysteresis response, low P_r , and single t/o diffraction peak. The pure HfO_2 and ZrO_2 films had diffraction patterns and electrical responses consistent with pure monoclinic and tetragonal phases, respectively. The high field permittivities (2.5 MV cm^{-1}), extracted from CV measurements (supplementary material, Fig. S3), further

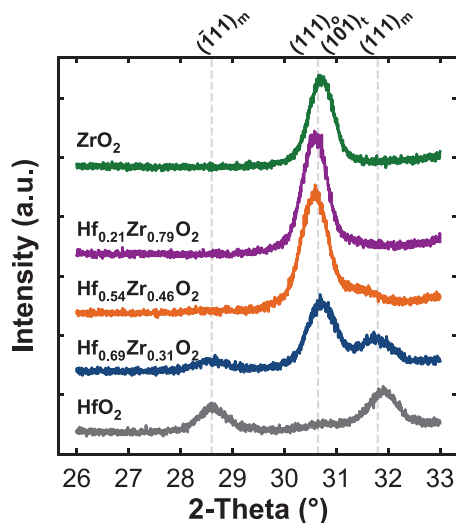


FIG. 2. GIXRD patterns measured on HfO_2 (gray), $\text{Hf}_{0.69}\text{Zr}_{0.31}\text{O}_2$ (blue), $\text{Hf}_{0.54}\text{Zr}_{0.46}\text{O}_2$ (orange), $\text{Hf}_{0.21}\text{Zr}_{0.79}\text{O}_2$ (purple), and ZrO_2 (green) films.

support a transition from a low permittivity monoclinic phase to higher permittivity orthorhombic and tetragonal phases as the film composition is varied from pure HfO_2 to pure ZrO_2 .

XRR measurements of each sample were used to quantify film densities and obtain thickness values. The measurements and associated fits can be found in the supplementary material, Figs. S4 and S5 for the crystallized and amorphous sample series, respectively. The densities of the crystallized and amorphous films were observed to decrease approximately linearly as the composition changed from pure HfO_2 to pure ZrO_2 , as provided in Table I and shown in the supplementary material, Fig. S6 along with the film thicknesses.

The longitudinal speed of sound was extracted from optical pump-probe picosecond acoustic measurements^{31–33} using a two-tint time-domain thermoreflectance system, which is described elsewhere.^{34,35} Briefly, the output of a Ti:sapphire oscillator (100 fs pulses, 80 MHz) is energetically separated into high-energy pump and low-energy probe paths. The pump is electro-optically modulated at 8.4 MHz and creates a periodic heating event at the surface of the

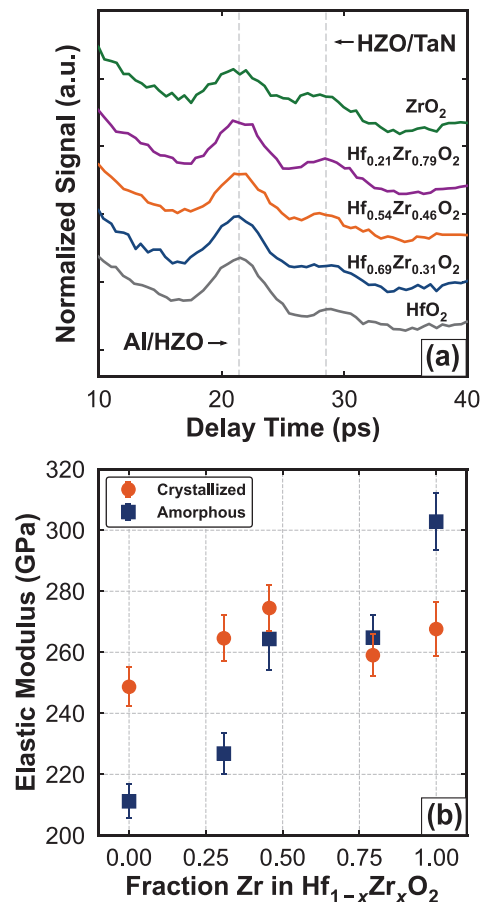


FIG. 3. (a) Acoustic responses measured on crystallized HfO_2 (gray), $\text{Hf}_{0.69}\text{Zr}_{0.31}\text{O}_2$ (blue), $\text{Hf}_{0.54}\text{Zr}_{0.46}\text{O}_2$ (orange), $\text{Hf}_{0.21}\text{Zr}_{0.79}\text{O}_2$ (purple), and ZrO_2 (green) films, with signatures corresponding to the Al/HZO and HZO/TaN interfaces indicated. (b) Elastic moduli calculated for crystallized (orange circles) and amorphous (blue squares) HZO films.

samples coated with aluminum. This heating event also generates a strain pulse that propagates through the film stack, partially transmitting/reflecting at the interfaces between the layers. The reflectivity of the aluminum transducer is interrogated using the probe, which is mechanically delayed ~ 100 ps following the incident pump pulse. Because the reflectivity of aluminum is proportional to both temperature and strain, signatures at short pump/probe delay times are indicative of the acoustic propagation times within each layer. Acoustic responses for the 20 nm-thick crystallized HZO films are shown in Fig. 3(a), where signatures from the Al/HZO and HZO/TaN interfaces are identified, with equivalent data for the amorphous films provided in the [supplementary material](#), Fig. S7. The delay time between these two signatures, τ , represents the round trip propagation time of the strain wave within the film, as diagramed in the [supplementary material](#), Fig. S8. Gaussian peaks were fit to both acoustic signatures to determine this delay, as shown for the $\text{Hf}_{0.54}\text{Zr}_{0.46}\text{O}_2$ film in the [supplementary material](#), Fig. S9. Utilizing the measured film thicknesses, d , and the round trip propagation times, the longitudinal speed of sound in each film was calculated via $v_L = 2d/\tau$. Elastic moduli were then calculated from the longitudinal wave velocities and the density measurements using the following equation with the assumptions of an isotropic randomly oriented, polycrystalline solid or isotropic amorphous layer:³⁶

$$E = \rho v_L^2, \quad (1)$$

where v_L is the longitudinal speed of sound, ρ is the film density, and E is the elastic modulus of the film. The elastic moduli, provided in Table I and shown in Fig. 3(b), were observed to increase with the increasing ZrO_2 composition, between 248 ± 6 GPa for the pure monoclinic HfO_2 film and 267 ± 9 GPa for the pure tetragonal ZrO_2 film, with positive deviations from this trend observed for the $\text{Hf}_{0.69}\text{Zr}_{0.31}\text{O}_2$ (264 ± 8 GPa) and $\text{Hf}_{0.54}\text{Zr}_{0.46}\text{O}_2$ (274 ± 8 GPa) compositions. The elastic moduli of the amorphous films were observed to increase upon increasing the ZrO_2 composition, from 211 ± 6 GPa to 302 ± 9 GPa between pure HfO_2 and pure ZrO_2 . Additional thickness, density, and sound velocity data for the amorphous films are provided in [supplementary material](#) Table SI.

Given that the $\text{Hf}_{0.69}\text{Zr}_{0.31}\text{O}_2$ and $\text{Hf}_{0.54}\text{Zr}_{0.46}\text{O}_2$ films contained the second largest and largest contents of the orthorhombic phase,

respectively, according to diffraction and electrical characterization, these positive deviations from the apparent increase indicate that the orthorhombic phase has an elastic modulus larger than the monoclinic and tetragonal phases. These values are in agreement with DFT predictions,^{37,38} and experimental trends between the bulk modulus of the monoclinic and non-ferroelectric orthorhombic phases of HfO_2 .³⁹ The elastic modulus measured for the $\text{Hf}_{0.54}\text{Zr}_{0.46}\text{O}_2$ film (274 ± 8 GPa), which possessed the largest content of the orthorhombic phase, is lower than the reported 340 GPa value extracted from fitting of acoustic vibrational responses of 10 nm-thick HZO nanomembrane resonators²⁷ and is larger than the reported ~ 170 GPa value measured on 10–100 nm-thick $\text{Hf}_{0.55}\text{Zr}_{0.45}\text{O}_2$ films by atomic force microscopy.⁴⁰ These differences may be related to varying phase purities, mechanical boundary conditions, and/or the indirect nature of moduli calculation from these other techniques.

Utilizing measured elastic moduli, $\sin^2(\psi)$ analyses were performed to assess the biaxial stress present in each of the crystalline films following processing. 2D diffraction patterns were collected using an area detector, with an example shown in Fig. 4(a) for the $\text{Hf}_{0.54}\text{Zr}_{0.46}\text{O}_2$ sample. Area detector data were unwarped using the MgO diffraction peaks, with an example shown in [supplementary material](#) Figure S10. The $(\bar{1}11)$ and (111) m (in the case of the HfO_2 film) and $(101)/(111)$ t/o reflections (in the case of the other films) were fit to quantify changes in d -spacing with the ψ angle relative to the film normal, as shown in Fig. 4(b) for the $\text{Hf}_{0.54}\text{Zr}_{0.46}\text{O}_2$ sample. The normalized intensities of the superimposed t/o diffraction peaks, also shown in Fig. 4(b) for the $\text{Hf}_{0.54}\text{Zr}_{0.46}\text{O}_2$ film, were observed to be effectively constant throughout the Debye ring, validating the assumption of a randomly oriented polycrystalline material. A similar lack of texture was observed in all other samples, except pure HfO_2 , with the 2D patterns shown in [supplementary material](#) Figure S11. These observed changes in d -spacing with the ψ angle were fit using Eqs. (2) and (3), with the assumption of a randomly oriented, polycrystalline solid with isotropic elastic behavior.⁴¹ Note that this calculation accounts for the biaxial modulus in an equi-biaxially stressed thin film,

$$\varepsilon_\psi = \frac{1 + \nu}{E} \sigma_\parallel \sin^2(\psi) - \frac{2\nu}{E} \sigma_\parallel, \quad (2)$$

TABLE I. Calculated elastic moduli and biaxial stress magnitudes along with parameters used for calculations, remanent polarizations, and relative permittivities for each HZO composition.

	HfO_2	$\text{Hf}_{0.69}\text{Zr}_{0.31}\text{O}_2$	$\text{Hf}_{0.54}\text{Zr}_{0.46}\text{O}_2$	$\text{Hf}_{0.21}\text{Zr}_{0.79}\text{O}_2$	ZrO_2
Thickness (nm)	20.04 ± 0.30	19.58 ± 0.29	19.37 ± 0.29	20.73 ± 0.31	21.60 ± 0.32
v_L (m s^{-1})	5392 ± 96	5788 ± 115	5984 ± 114	6164 ± 110	6656 ± 151
τ (ps)	7.43 ± 0.07	6.76 ± 0.09	6.47 ± 0.08	6.72 ± 0.07	6.37 ± 0.11
ρ (g cm^{-3})	8.55 ± 0.03	7.90 ± 0.04	7.67 ± 0.04	6.82 ± 0.06	6.04 ± 0.05
P_r ($\mu\text{C cm}^{-2}$, at 2.5 MV cm^{-1})	0.54	8.38	14.01	2.82	0.03
ε_r (at 2.5 MV cm^{-1} , 10 kHz)	23.6	34.1	51.1	60.3	42.7
E (GPa, Amorphous)	211 ± 6	226 ± 7	267 ± 10	264 ± 8	302 ± 9
E (GPa, Crystallized)	248 ± 6^a	264 ± 8	274 ± 8	259 ± 7	267 ± 9
σ (GPa)	$2.54 \pm 0.6^{a,b}$	3.75 ± 0.2	4.71 ± 0.4	5.00 ± 0.3	5.22 ± 0.5

^a HfO_2 area detector data indicate the preferred orientation.

^bThe value represents the average of calculations from both $(\bar{1}11)$ and (111) monoclinic peaks.

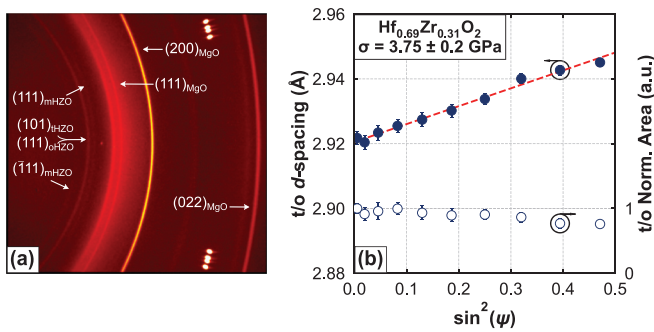


FIG. 4. (a) 2D XRD pattern measured on the $\text{Hf}_{0.69}\text{Zr}_{0.31}\text{O}_2$ sample with indexed m, t/o, and MgO Debye rings indicated. (b) Change in t/o d -spacing with the ψ angle relative to the film normal (filled blue circles, left axis) with an associated linear fit (red dotted line) used to calculate biaxial stress magnitude and normalized peak intensities (open blue circles, right axis) for the $\text{Hf}_{0.69}\text{Zr}_{0.31}\text{O}_2$ film.

$$\epsilon_{\psi} = \frac{d_{\psi} - d_0}{d_0}, \quad (3)$$

where d_{ψ} is the d -spacing at each ψ angle, ν is Poisson's ratio (assumed to be 0.29^{42–44}), E is the measured elastic modulus for each composition, and σ_{\parallel} is the biaxial stress state. The strain-free d -spacings (d_0) of the HZO films were calculated to occur at ψ angles (ψ^*) at which the following equation was fulfilled:⁴¹

$$\sin(\psi^*) = \sqrt{\frac{2\nu}{1+\nu}}. \quad (4)$$

The d -spacings of the MgO powder resting on the film surface, shown in the [supplementary material](#), Figs. S10 and S12, were not observed to vary with the ψ angle, indicating that the observed m/t/o d -spacing slopes are not measurement artifacts.

The biaxial stress states of the crystalline films were found to be 2.54 ± 0.6 GPa for the pure HfO_2 film (averaged between the $(\bar{1}11)$ and (111) monoclinic peaks), 3.75 ± 0.2 GPa, 4.71 ± 0.4 GPa, and 5.00 ± 0.3 GPa for the $\text{Hf}_{0.69}\text{Zr}_{0.31}\text{O}_2$, $\text{Hf}_{0.54}\text{Zr}_{0.46}\text{O}_2$, and $\text{Hf}_{0.21}\text{Zr}_{0.79}\text{O}_2$ compositions, respectively, and 5.22 ± 0.5 GPa for the ZrO_2 film. Values utilized for stress quantification can be found in [Table I](#), a discussion of error propagation in all elastic moduli and biaxial stress calculations can be found in the [supplementary material](#), and analogous $\sin^2(\psi)$ analyses can be found for the other samples in the [supplementary material](#), Fig. S13. The large tensile biaxial stresses present following processing are consistent with other studies examining stress states of HfO_2 -based ferroelectrics grown on binary nitride electrodes and suggest significant stress resulting from the thermal expansion mismatch with the silicon substrates.²⁴ Given that monoclinic HfO_2 possesses a smaller coefficient of thermal expansion than tetragonal ZrO_2 ⁴⁵ and that clear evidence of monoclinic ferroelastic twin texturing was observed in the 2D diffraction patterns,⁴⁶ it is anticipated that the monoclinic HfO_2 and mixed phase $\text{Hf}_{0.69}\text{Zr}_{0.31}\text{O}_2$ films could better accommodate thermal strains compared to the other compositions and, thus, maintain lower biaxial stress following processing. The texture of the $(\bar{1}11)$ and (111) reflections in the pure HfO_2 film does mean that the assumption of a randomly oriented, isotropic crystalline solid used throughout the stress calculations is less valid for this film than for the other compositions. Furthermore, it should be

emphasized that all the crystal structures present in this study are elastically anisotropic. An implicit assumption of the $\sin^2(\psi)$ technique used is that the elastic properties of the planes considered do not significantly differ. The complete elastic compliance tensor for each phase and composition would be necessary to account for any differences, and, to date, this information is not available. Regardless, the random orientation of most compositions, linearity of d -spacing vs $\sin^2(\psi)$, and the use of the same atomic plane in each phase suggest that these results are reliable.

In summary, the elastic moduli of amorphous and crystalline 20 nm-thick $\text{Hf}_{1-x}\text{Zr}_x\text{O}_2$ films have been directly quantified using picosecond acoustic measurements. For the crystallized films, the elastic moduli were found to increase from 248 ± 6 GPa to 267 ± 9 GPa between the monoclinic HfO_2 and tetragonal ZrO_2 films, respectively. The $\text{Hf}_{0.69}\text{Zr}_{0.31}\text{O}_2$ and $\text{Hf}_{0.54}\text{Zr}_{0.46}\text{O}_2$ films, which were determined to have the largest content of orthorhombic phase, exhibited larger elastic moduli of 264 ± 8 GPa and 274 ± 8 GPa, respectively. The larger elastic moduli of films containing the orthorhombic phase are consistent with computational predictions. The moduli of the amorphous films were observed to linearly increase between 211 ± 6 GPa and 302 ± 9 GPa as the composition was varied from pure HfO_2 to pure ZrO_2 . The biaxial stresses of the crystalline films, quantified using their measured elastic modulus values through $\sin^2(\psi)$ analysis, were found to increase from 2.54 ± 0.6 GPa, for pure HfO_2 , to 5.22 ± 0.5 GPa, for pure ZrO_2 . Direct investigation of these elastic properties, through utilization of picosecond acoustic measurements, allows for enhanced analysis of stress effects on the phase stability, domain structure, and polarization properties in HfO_2 -based ferroelectric thin films.

See the [supplementary material](#) for a detailed description of the PEALD processing, XPS measurements, error propagation, and supplemental figures.

This work was supported, in part, by the Laboratory Directed Research and Development program at Sandia National Laboratories. Sandia National Laboratories is a multimission laboratory managed and operated by the National Technology and Engineering Solutions of Sandia, LLC, a wholly owned subsidiary of Honeywell International, Inc., for the U.S. Department of Energy's National Nuclear Security Administration under Contract No. DE-NA0003525. This paper describes objective technical results and analysis. Any subjective views or opinions that might be expressed in this paper do not necessarily represent the views of the U.S. Department of Energy or the United States Government. This work was also supported, in part, by the Semiconductor Research Corporation's (SRC) Global Research Collaboration Program. This research utilized a PHI VersaProbe III XPS system, which was supported by National Science Foundation Award No. 162601. S.T.J. acknowledges support from the National Science Foundation Graduate Research Fellowship Program under Award No. DGE-1842490. D.H.O. is grateful for funding from the National Defense Science and Engineering Graduate (NDSEG) Fellowship. D.H.O. and P.E.H. appreciate funding from the National Science Foundation, Grant No. DMR EPM 2006231. This manuscript was coauthored by UT-Battelle, LLC, under Contract No. DE-AC05-00OR22725 with the U.S. Department of Energy. The United States Government retains and the publisher, by accepting this article for

publication, acknowledges that the United States Government retains a non-exclusive, paid-up, irrevocable, world-wide license to publish or reproduce the published form of this manuscript, or allow others to do so, for United States Government purposes.

DATA AVAILABILITY

The data that support the findings of this study are available within this article and its [supplementary material](#).

REFERENCES

- ¹T. S. Böscke, J. Müller, D. Bräuhäus, U. Schröder, and U. Böttger, *Appl. Phys. Lett.* **99**, 102903 (2011).
- ²S. Mueller, S. R. Summerfelt, J. Muller, U. Schroeder, and T. Mikolajick, *IEEE Electron Device Lett.* **33**, 1300 (2012).
- ³J. Müller, T. S. Böscke, D. Bräuhäus, U. Schröder, U. Böttger, J. Sundqvist, P. Kücher, T. Mikolajick, and L. Frey, *Appl. Phys. Lett.* **99**, 112901 (2011).
- ⁴L. Chen, T.-Y. Wang, Y.-W. Dai, M.-Y. Cha, H. Zhu, Q.-Q. Sun, S.-J. Ding, P. Zhou, L. Chua, and D. W. Zhang, *Nanoscale* **10**, 15826 (2018).
- ⁵Y. Goh and S. Jeon, *Nanotechnology* **29**, 335201 (2018).
- ⁶S. Kirbach, K. Kühnel, and W. Weinreich, in 2018 IEEE 18th International Conference on Nanotechnology (IEEE-NANO) (2018), pp. 1–4.
- ⁷M. Hoffmann, U. Schroeder, C. Künne, A. Kersch, S. Starschich, U. Böttger, and T. Mikolajick, *Nano Energy* **18**, 154 (2015).
- ⁸M. Hoffmann, B. Max, T. Mittmann, U. Schroeder, S. Slesazeck, and T. Mikolajick, in 2018 IEEE International Electron Devices Meeting (IEDM) (2018), p. 31.6.1–31.6.4.
- ⁹M. Hoffmann, F. P. G. Fengler, M. Herzig, T. Mittmann, B. Max, U. Schroeder, R. Negrea, P. Lucian, S. Slesazeck, and T. Mikolajick, *Nature* **565**, 464 (2019).
- ¹⁰R. Batra, T. D. Huan, G. A. Rossetti, and R. Ramprasad, *Chem. Mater.* **29**, 9102 (2017).
- ¹¹R. Batra, T. D. Huan, J. L. Jones, G. Rossetti, and R. Ramprasad, *J. Phys. Chem. C* **121**, 4139 (2017).
- ¹²C. Künne, R. Materlik, and A. Kersch, *J. Appl. Phys.* **121**, 205304 (2017).
- ¹³S. Starschich and U. Böttger, *J. Mater. Chem. C* **5**, 333 (2017).
- ¹⁴M. H. Park, T. Schenk, C. M. Fancher, E. D. Grimley, C. Zhou, C. Richter, J. M. LeBeau, J. L. Jones, T. Mikolajick, and U. Schroeder, *J. Mater. Chem. C* **5**, 4677 (2017).
- ¹⁵S. J. Kim, D. Narayan, J.-G. Lee, J. Mohan, J. S. Lee, J. Lee, H. S. Kim, Y.-C. Byun, A. T. Lucero, C. D. Young, S. R. Summerfelt, T. San, L. Colombo, and J. Kim, *Appl. Phys. Lett.* **111**, 242901 (2017).
- ¹⁶T. Shiraishi, K. Katayama, T. Yokouchi, T. Shimizu, T. Oikawa, O. Sakata, H. Uchida, Y. Imai, T. Kiguchi, T. J. Konno, and H. Funakubo, *Appl. Phys. Lett.* **108**, 262904 (2016).
- ¹⁷J. Müller, T. S. Böscke, U. Schröder, S. Mueller, D. Bräuhäus, U. Böttger, L. Frey, and T. Mikolajick, *Nano Lett.* **12**, 4318 (2012).
- ¹⁸M. H. Park, H. J. Kim, Y. J. Kim, Y. H. Lee, T. Moon, K. D. Kim, S. D. Hyun, F. Fengler, U. Schroeder, and C. S. Hwang, *ACS Appl. Mater. Interface* **8**, 15466 (2016).
- ¹⁹H. A. Hsain, Y. Lee, G. Parsons, and J. L. Jones, *Appl. Phys. Lett.* **116**, 192901 (2020).
- ²⁰H. Yu, C.-C. Chung, N. Shewmon, S. Ho, J. H. Carpenter, R. Larrabee, T. Sun, J. L. Jones, H. Ade, B. T. O'Connor, and F. So, *Adv. Funct. Mater.* **27**, 1700461 (2017).
- ²¹S. W. Smith, A. R. Kitahara, M. A. Rodriguez, M. D. Henry, M. T. Brumbach, and J. F. Ihlefeld, *Appl. Phys. Lett.* **110**, 072901 (2017).
- ²²E. A. Scott, S. W. Smith, M. D. Henry, C. M. Rost, A. Giri, J. T. Gaskins, S. S. Fields, S. T. Jaszewski, J. F. Ihlefeld, and P. E. Hopkins, *Appl. Phys. Lett.* **113**, 192901 (2018).
- ²³T. Shiraishi, K. Katayama, T. Yokouchi, T. Shimizu, T. Oikawa, O. Sakata, H. Uchida, Y. Imai, T. Kiguchi, T. J. Konno, and H. Funakubo, *Mater. Sci. Semicond. Process.* **70**, 239 (2017).
- ²⁴T. Schenk, C. M. Fancher, M. H. Park, C. Richter, C. Künne, A. Kersch, J. L. Jones, T. Mikolajick, and U. Schroeder, *Adv. Electron. Mater.* **5**, 1900303 (2019).
- ²⁵E. D. Grimley, T. Schenk, X. Sang, M. Pešić, U. Schroeder, T. Mikolajick, and J. M. LeBeau, *Adv. Electron. Mater.* **2**, 1600173 (2016).
- ²⁶M. Ghatge, G. Walters, T. Nishida, and R. Tabrizian, *Appl. Phys. Lett.* **116**, 043501 (2020).
- ²⁷F. Hakim, M. Ghatge, and R. Tabrizian, *Appl. Phys. Lett.* **117**, 063502 (2020).
- ²⁸B. H. Toby and R. B. Von Dreele, *J. Appl. Crystallogr.* **46**, 544 (2013).
- ²⁹G. Esteves, K. Ramos, C. M. Fancher, and J. L. Jones, *LIPRAS: Line-Profile Analysis Software* (MathWorks, 2020).
- ³⁰J. Kieffer, V. Valls, N. Blanc, and C. Hennig, *J. Synchrotron Radiat.* **27**, 558 (2020).
- ³¹J. L. Braun, S. W. King, A. Giri, J. T. Gaskins, M. Sato, T. Fujiseki, H. Fujiwara, and P. E. Hopkins, *Appl. Phys. Lett.* **109**, 191905 (2016).
- ³²C. Thomsen, H. J. Maris, and J. Tauc, *Thin Solid Films* **154**, 217 (1987).
- ³³H. -N. Lin, R. J. Stoner, H. J. Maris, and J. Tauc, *J. Appl. Phys.* **69**, 3816 (1991).
- ³⁴K. Kang, Y. K. Koh, C. Chiritescu, X. Zheng, and D. G. Cahill, *Rev. Sci. Instrum.* **79**, 114901 (2008).
- ³⁵D. H. Olson, J. T. Gaskins, J. A. Tomko, E. J. Opila, R. A. Golden, G. J. K. Harrington, A. L. Chamberlain, and P. E. Hopkins, *Scr. Mater.* **177**, 214 (2020).
- ³⁶R. Newnham, *Properties of Materials: Anisotropy, Symmetry, Structure* (Oxford University Press, 2005).
- ³⁷R. Materlik, C. Künne, and A. Kersch, *J. Appl. Phys.* **117**, 134109 (2015).
- ³⁸M. H. Park, Y. H. Lee, H. J. Kim, T. Schenk, W. Lee, K. D. Kim, F. P. G. Fengler, T. Mikolajick, U. Schroeder, and C. S. Hwang, *Nanoscale* **14**, 9973 (2017).
- ³⁹Y. Al-Khatatbeh, K. K. M. Lee, and B. Kiefer, *Phys. Rev. B* **82**, 144106 (2010).
- ⁴⁰L. Bolotov, N. Uchida, and S. Migita, *AIP Adv.* **11**, 015216 (2021).
- ⁴¹M. Birkholz, *Thin Film Analysis by X-Ray Scattering* (Wiley-VCH, KGaA, Weinheim, 2006).
- ⁴²S. L. Dole, O. Hunter, and C. J. Wooge, *J. Am. Ceram. Soc.* **60**, 488 (1977).
- ⁴³X.-S. Zhao, S.-L. Shang, Z.-K. Liu, and J.-Y. Shen, *J. Nucl. Mater.* **415**, 13 (2011).
- ⁴⁴A. SelCuk and A. Atkinson, *J. Eur. Ceram. Soc.* **17**, 1523 (1997).
- ⁴⁵R. P. Haggerty, P. Sarin, Z. D. Apostolov, P. E. Driemeyer, and W. M. Kriven, *J. Am. Ceram. Soc.* **97**, 2213 (2014).
- ⁴⁶B. M. Hudak, S. W. Depner, G. R. Waetzig, A. Talapatra, R. Arroyave, S. Banerjee, and B. S. Guiton, *Nat. Commun.* **8**, 15316 (2017).